JGR Space Physics

RESEARCH ARTICLE
10.1029/2018JA026333

Multispectral and Multi-instrument Observation of TIDs Following the Total Solar Eclipse of 21 August 2017

Saurav Aryal[1], George Geddes[1], Susanna C. Finn[1], Sebastijan Mrak[2], Ivan Galkin[1], Ingrid Cnossen[3,4], Timothy Cook[1], and Supriya Chakrabarti[1]

[1]Lowell Center for Space Science and Technology (LoCSST), Department of Physics and Applied Physics, University of Massachusetts Lowell, Lowell, MA, USA, [2]Department of Electrical and Computer Engineering and Center for Space Physics, Boston University, Boston, MA, USA, [3]Department of Climate and Space Sciences and Engineering, University of Michigan, Ann Arbor, MI, USA, [4]British Antarctic Survey, Cambridge, UK

Key Points:
- Meridional and vertical wave properties of LSTIDs are characterized based on multi-instrument observations
- Effects of the solar eclipse that preceded the LSTID are also studied based on modeling
- Model estimates suggest that the IT system was preconditioned due to the eclipse but there is no evidence of this affecting the LSTIDs

Supporting Information:
- Movie S1
- Figure S1
- Figure S2

Correspondence to:
S. Aryal,
saurav_aryal@student.uml.edu

Citation:
Aryal, S., Geddes, G., Finn, S. C., Mrak, S., Galkin, I., Cnossen, I., et al. (2019). Multispectral and multi-instrument observation of TIDs following the total solar eclipse of 21 August 21, 2017. *Journal of Geophysical Research: Space Physics*, *124*, 3761–3774. https://doi.org/10.1029/2018JA026333

Received 3 DEC 2018
Accepted 13 APR 2019
Accepted article online 22 APR 2019
Published online 25 MAY 2019

Abstract Wave-like structures in the upper atmospheric nightglow brightness were observed on the night of 22 August 2017, approximately 8 hr following a total solar eclipse. These wave-like perturbations are signatures of atmospheric gravity waves and associated traveling ionospheric disturbances (TIDs). Observations were made in the red line (OI 630.0 nm) and the green line (OI 557.7 nm) from Carbondale, IL, at 2–10 UTC on 22 August 2017. Based on wavelet analyses, the dominant time period in both the red and green lines was around 1.5 hr. Differential total electron content data obtained from Global Positioning System total electron content measurements at Carbondale, IL, and ionospheric parameters from digisonde measurements at Idaho National Laboratory and Millstone Hill showed a similar dominant time period. Based on these observations and their correlation with geomagnetic indices, the TIDs appear to be associated with geomagnetic disturbances. In addition, by modeling the ionosphere-thermosphere system's response to the eclipse, it was seen that while the eclipse enhanced the O/N_2 ratio and electron density (N_e) at 250 km during our observation period, it did not affect the TIDs. Vertical (7 m/s) and meridional (616 m/s) phase velocities of the TIDs were estimated using cross-correlation analysis between red and green line brightness profiles and spectral analysis of the differential total electron content keogram, respectively. This provides a method to characterize the three-dimensional wave properties of TIDs.

1. Introduction

Atmospheric gravity waves (AGWs) manifest as traveling ionospheric disturbances (TIDs) via ion-neutral coupling in the ionosphere-thermosphere (IT) system (Hines, 1960). TIDs are wave-like plasma oscillations in the ionosphere that can be triggered by various processes (including AGWs) and occur at different temporal and spatial scales. TIDs with wavelengths of 100–300 km are classified as medium-scale TIDs and can be caused by various processes but in general are associated with tropospheric forcing (Kelley, 2011). TIDs with wavelengths larger than 1,000 km and with time periods greater than 1 hr are classified as large-scale TIDs (LSTIDs; Hocke & Schlegel, 1996).

Most LSTIDs propagate from either pole and are associated with magnetic disturbances. Geomagnetic storms cause rapid enhancement of the auroral electrojet that leads to thermospheric heating and expansion (Chimonas & Hines, 1970b; Davis, 1971). This generates AGWs that propagate toward the equator. The divergence of AGWs in turn generates LSTIDs (Prölss & Ocko, 2000). LSTIDs that have propagated equatorward and are associated with geomagnetic storms have been observed by previous studies (Habarulema et al., 2018, and references therein). For example, based on magnetometer measurements, Habarulema et al. (2018) showed that equatorward TIDs were launched following a southward turning of the interplanetary magnetic field (IMF).

Besides geomagnetic storms, solar eclipses are also known to excite AGWs (e.g., Chimonas & Hines, 1970a; Liu et al., 1998) that alter the IT system (Harding et al., 2018; Lin et al., 2018). Liu et al. (1998) conclude that the ionospheric perturbations that they observed using ionosondes during the total solar eclipse of 24 October 1995 were most likely due to plasma upflow and downflow induced by rapid temperature increase immediately following the eclipse.

The 21 August 2017 solar eclipse occurred over the continental United States (from the West to the East Coast) where numerous satellite receivers and ground-based instruments were present, leading to an abundance of data for studying the effects on the upper atmosphere. Coster et al. (2017) found signatures of possible mountain waves, using total electron content (TEC) maps, during the 21 August 2017 eclipse. Furthermore, for the same eclipse event, Goncharenko et al. (2018) used colocated measurements of digisonde and the Millstone Hill (MH) ISR (Westford, MA, ~60% peak obscuration) and observed a fast (20–40 m/s) upward plasma drift above the peak height of the *F*2 layer, *hmF*2, immediately following the maximum obscuration which they attributed to rapid temperature increase. Neutral wind velocity derived from nighttime OI 630.0 nm (red line) emission measurements by a Fabry-Perot interferometer in Brazil showed perturbations in neutral winds far from the path of the 21 August 2017 eclipse. Global-scale simulations using an ultraviolet obscuration mask that mimicked the 21 August 2017 eclipse's effect on the upper atmosphere successfully predicted the measured changes (using the red line) in neutral wind qualitatively (Harding et al., 2018).

On 22 August 2017 a sequence of LSTIDs was observed in the Northern Hemisphere, following a minor geomagnetic storm (minimum Dst index ~ -30 nT, peak Auroral Electrojet index ~1,000 nT) over North America. The geomagnetic storm followed the eclipse of 21 August 2017 that occurred hours earlier. In this paper, we present a comprehensive LSTID analysis, by virtue of simultaneous measurements by ground-based spectral imager (at Carbondale, IL, which was in the path of totality), Global Positioning System (GPS) differential TEC maps, and high-cadence ionospheric characteristics provided by digisondes. We describe the TID event analysis in detail and characterize the TID wave parameters. In addition, we compare our observations to simulations with the Global Ionosphere-Thermosphere Model (GITM; Ridley et al., 2006) to examine if the solar eclipse affected the observed TIDs.

2. Measurements

2.1. Spectral Measurements

Our observations of the TIDs from Carbondale, IL, (geographic location: 37.7°N, 89.2°W) were made using the High Throughput and Multi-slit Imaging Spectrograph (HiT&MIS; Chakrabarti et al., 2012). HiT&MIS can simultaneously measure six upper atmospheric emission features at high resolution (dispersion of ~0.02 nm/pixel in red line, for example). The field of view (FOV) of HiT&MIS is approximately 0.1° by 50° and was centered at an elevation angle of 45° looking toward the northwest (Figure 1). The spectral images were recorded at a cadence of 4 min using a charged coupled device (CCD) camera during 2–10 UTC on 22 August 2017. Simultaneous measurements in the red line and OI 557.7 nm (green line) are used for this particular study.

From the raw charged coupled device images, wavelength regions around the red and green lines, plus a diagnostic cloud indicator also observed by HiT&MIS, were extracted as a function of HiT&MIS elevation angle and wavelength. The NeI 630.5-nm line (present in street lights) was used as an indicator of cloud activity as reflection of street lights from clouds acts as a proxy for sky conditions. See Aryal et al. (2018) for a more detailed description of the spectra extraction procedure for HiT&MIS.

For each feature at each time stamp, we obtained the brightness by coadding signals from all wavelength bins around ±0.3 nm from the line center. We then plotted the brightness as a function of elevation angle and time. GLobal airglOW (Bailey et al., 2002; Solomon & Abreu, 1989; Solomon et al., 1988) model estimates of the volume emission rate (Figure 2) provided the peak heights of the red (250 km) and green (220 km) lines in the nighttime thermosphere (Figure 2). Using these emission heights and the viewing geometry of HiT&MIS, the elevation angles were then converted to the latitude of the emission height projected on the ground.

2.2. GPS Differential TEC Measurements

In order to compare the airglow brightness morphologies in the spectral data, we used the differential total electron content (DTEC) maps. We used Continuously Operating Reference Stations (www.ngs.noaa.gov/CORS) and Crustal Dynamics Data Information System (cddis.nasa.gov) publicly available databases with Global Navigation Satellite Systems observation data. This accounted for a total of ~1,800 receivers in the continental United States.

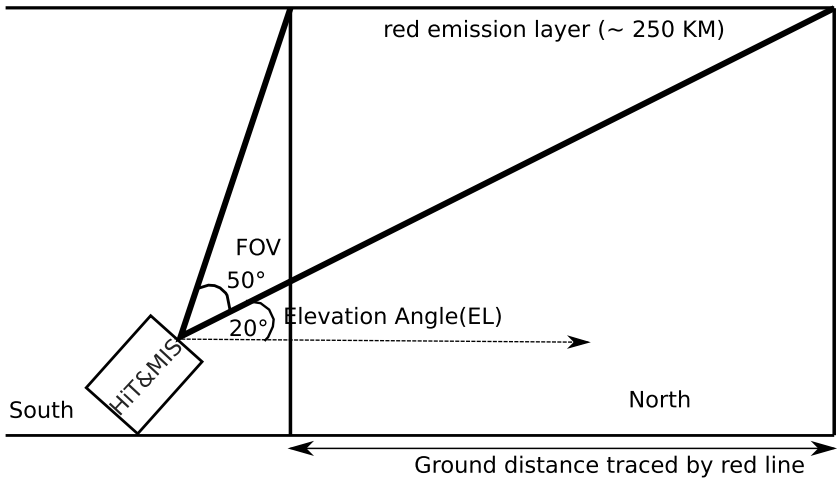

Figure 1. Viewing geometry of the HiT&MIS instrument on 21–22 August 2017 at Carbondale, IL. The latitudes (and ground distance) traced by the red line are shown assuming the peak emission height of 250 km. HiT&MIS = High Throughput and Multi-slit Imaging Spectrograph.

To compute the phase-corrected slant TEC estimates, we used the approach of Coster et al. (1992). The slant TEC was converted to the vertical TEC via a mapping function applied at 300-km altitude (Klobuchar, 1987). We then subtracted the background vertical TEC to obtain DTEC residuals, using variable orders of polynomials (cf. Mrak et al., 2018). The carrier phase-based differential approach provides an accuracy better than 0.03 TECu (Coster et al., 2012; 1 TECu = 10^{16}e^{-}/m^{2}), which enables one to resolve tiny but spatially coherent perturbations in TEC. The DTEC residuals were mapped to a geographical map at an altitude of 300 km and transformed from the naturally irregular spatial grid into a regular grid (e.g., Azeem et al., 2015; Mrak et al., 2018) with a resolution of 0.2° × 0.2° (geographical coordinates). Due to the size of the grid (spatial sampling) and slant-to-vertical mapping uncertainty, the minimum scale sizes that can be inferred from these maps are on the order of 100 km. For example, Mrak et al. (2018) demonstrated detection of TIDs

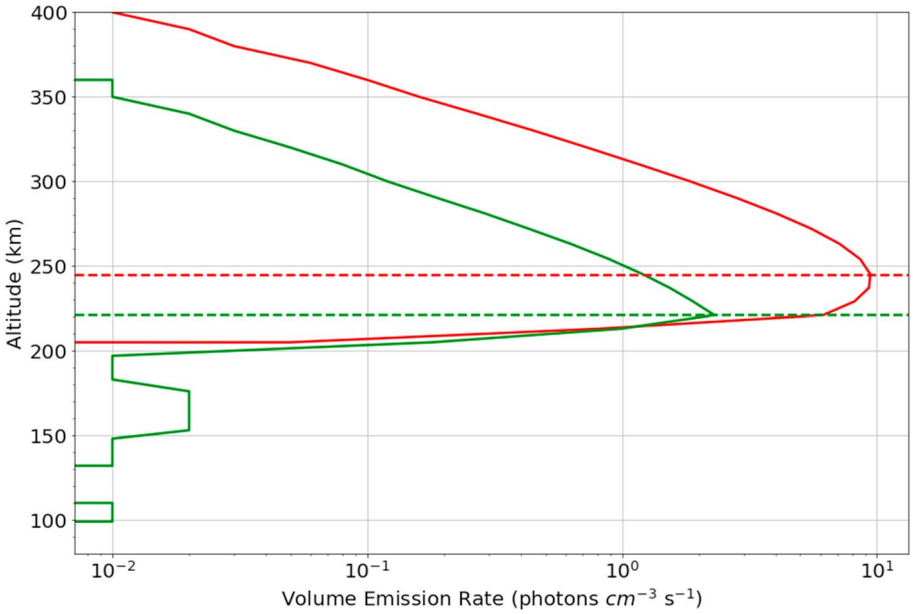

Figure 2. The volume emission rate for the red and green lines as modeled by GLobal airglOW at 4 UTC on 22 August 2017. MSIS00 and IRI-90 empirical parameters were used for neutral and plasma profiles, respectively.

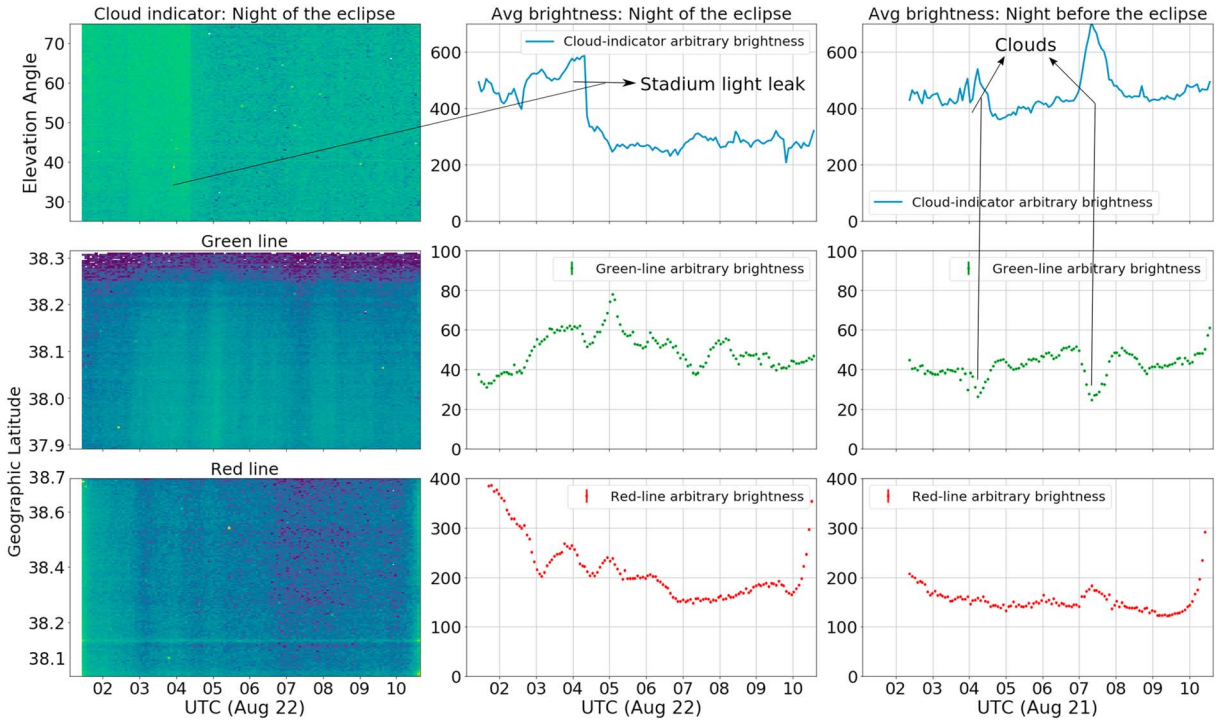

Figure 3. (left column) Brightness keogram of Ne I (cloud indicator, top), green line (middle), and red line (bottom) as a function of look direction (or latitude) on the night of the eclipse (22 August). Brighter color represents higher brightness (in arbitrary units). Section 2.1 describes how the look directions are converted to latitudes. (middle column) Brightness averaged over the whole field of view (0.1° by 50°) for each representative keogram on the left. Notice clear wave-like perturbations seen in both red and green lines on 22 August. (right column) Same as the middle column but on the night before the eclipse (21 August, keogram not shown). Note: as no photometric calibration was done and since the sensitivity of the instrument is not the same at different spectral region, red and green brightnesses cannot be compared. That is, green line arbitrary brightness of 40 could be brighter than the red line arbitrary brightness of 100. UTC = universal time coordinated.

at wavelengths of 200–300 km. We extracted the DTEC time series observations for locations aligned with the HiT&MIS FOV at the assumed altitude.

2.3. Digisonde Measurements

An additional insight into the nature of observed TIDs is provided by the Global Ionosphere Radio Observatory (Reinisch & Galkin, 2011), a network of *ionosondes*, high-frequency bottomside ionosphere sounders. We selected two Global Ionosphere Radio Observatory locations operated by Idaho National Laboratory (INL) at Idaho Falls, ID (43.5°N, 112°W) and by the University of Massachusetts Lowell at MIT Haystack Observatory, MH (42.5°N, 71.4°W). Both observatories employed the latest Digisonde model DPS4D (Lowell Digisonde International, (LDI), 2018; Reinisch et al., 2009) in its high-cadence campaign mode, recording the vertical sounding ionograms once a minute.

Since the first report of the TID phenomenon detected by means of high-frequency radio interferometry (Munro, 1950), ionosondes have been used as reliable TID detectors with well-established sensitivity to plasma perturbations, as even minute changes of the electron density cause easily detectable variability of the signal propagation path in the ionosphere. For our investigation, we used time series of the Maximum Usable Frequency (MUF) at a distance of 3,000 km (D), MUF (D)*F*2, an URSI standard ionogram-derived characteristic. MUF(D)*F*2 (referred to as MUF hereafter) is obtained numerically using the shape of the O-wave signal trace extracted from the vertical ionogram (see Davies, 1989, for details) and its change reflects variability in both peak density and height of the *F*2 layer (see supporting information Figure S1). This thus enhances the overall sensitivity to plasma perturbations in comparison to individual analysis of the ionospheric characteristics describing density, reflection height, or columnar content of the ionosphere. The efficiency of the ionogram-derived MUF variation analysis for TID diagnostics was recently the subject of

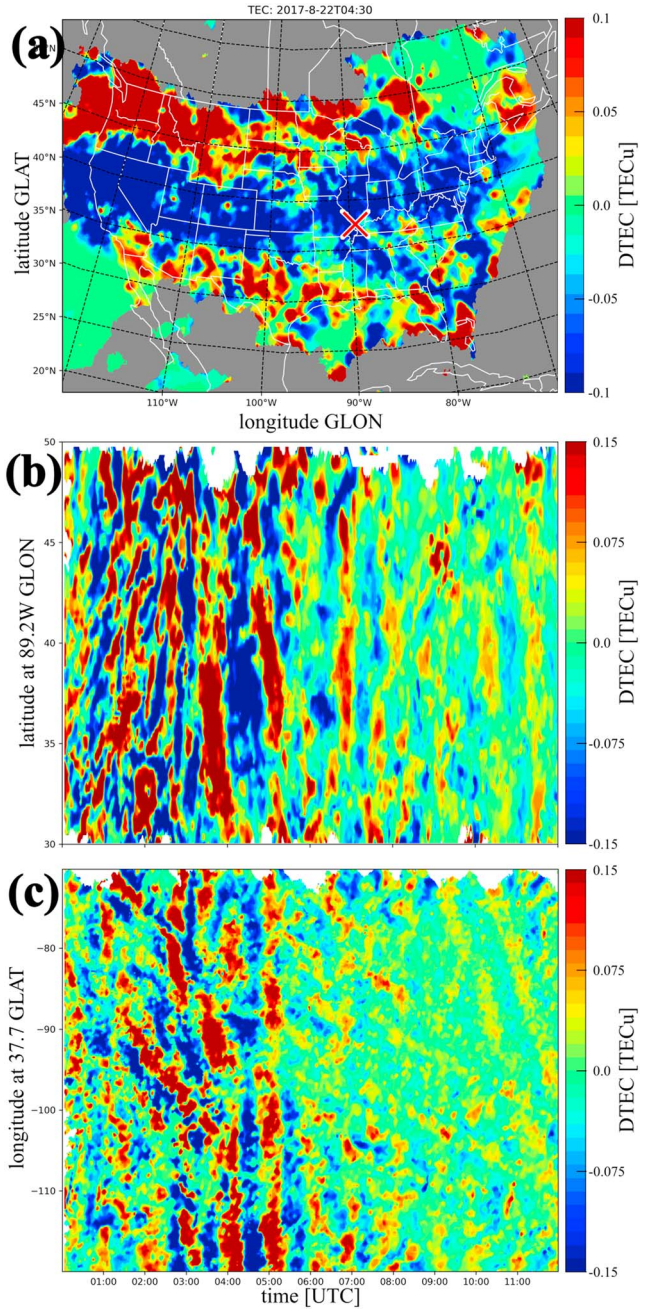

Figure 4. The large-scale traveling ionospheric disturbance event as observed by Global Positioning System-aided DTEC maps. (a) A representative DTEC map of traveling ionospheric disturbances over continental United States at 4:30 UTC. The red "X" mark denotes the location of the High Throughput and Multi-slit Imaging Spectrograph instrument at Carbondale, IL (37.7°N, 89.2°W). (b) A DTEC keogram elongated along 89.2°W longitude. (c) A DTEC keogram elongated along 37.7°N latitude. TEC = total electron content; DTEC = differential total electron content; UTC = universal time coordinated, GLAT = Geographic Latitude, GLON = Geographic Longitude.

a multi-instrument cross-validation study as a part of the TID warning and mitigation project TechTIDE (Altadill et al., 2018).

3. Results

3.1. Spectral Data

The red and green line brightnesses for the night of the eclipse and TID event (22 August 2017) are presented in Figure 3. The brightness data for the night before the eclipse (21 August 2017) are also shown for comparison. The red and green line brightnesses on the night with the TID event (22 August) show wave-like brightness perturbations, while the perturbations on the night before (21 August) only coincide with the cloud indicator, especially in the green line. A slightly positive coincidence is seen in the red line possibly because the wings of the NeI 630.5-nm spectra leak into the red line (630.0 nm). There is a sudden drop in the cloud indicator brightness around 4 UTC on 22 August; this is due to nearby stadium light, which was in HiT&MIS FOV, being switched off. The cloud indicator brightness on 22 August is around the same level as 21 August even with the stadium light on and lower after the stadium light was turned off. This suggests that the sky on 22 August 2017 (night of the TID event) was relatively cloud free near HiT&MIS's FOV.

3.2. DTEC Data

To validate the wave-like brightness perturbation seen in the spectral data, DTEC maps over the continental United States were used. Figure 4 shows an example of the GPS-derived DTEC maps and a set of keograms crossing the location of the HiT&MIS instrument. Figure 4a shows the geographical extent of the large-scale perturbations at 4:30 UTC, when the geomagnetic activity was already in the recovery phase. The LSTIDs are longitudinally uniform in longitudes west of ~ 100°W, whereas further east they are generally latitudinally uniform. About 100°W is where approximate line of geomagnetic declination angle 0° lies, and so the observed structures could be associated with it. Further, keograms in Figures 4b and 4c show the temporal extent of the LSTIDs in the meridional and zonal direction above the HIT&MIS location. The peak TID activity was observed in the time range of 3–6 UT. Figure 5 shows concurrent, coaligned time series of DTEC and the dynamic part of the red and green line profiles obtained by polynomial detrending at Carbondale, IL. The perturbations in the DTEC and in the green and red line brightnesses coincide at 3–6 UTC, which is also the time period when significant large-scale perturbations were observed in the DTEC keogram (Figure 4).

3.3. Digisonde MUF Data

To further verify the large-scale nature of the observed TIDs, we used digisonde-derived MUF series from two far away locations. Figure 6 shows the MUF timelines at MH and INL from 19 UTC on 21 August 2017 to 6 UTC 22 August 2017. The MUF variability is significant at both locations. Perturbations are also seen immediately prior to the start of geomagnetic disturbances (0 UTC on 22 August 2017). These premidnight perturbations might be associated with the aftereffect of the eclipse, as Goncharenko et al. (2018) also reported enhanced plasma density over MH around 21 UTC (21 August) based on radar measurements. Goncharenko et al. (2018) attributed these enhancements to the eclipse's aftereffect. On the other hand, the postmidnight DTEC, red and green line brightnesses and MUF dynamics were more likely associated with the TIDs generated due to an increase in auroral currents as a result of enhanced geomagnetic activity. We expand on this further in the following section.

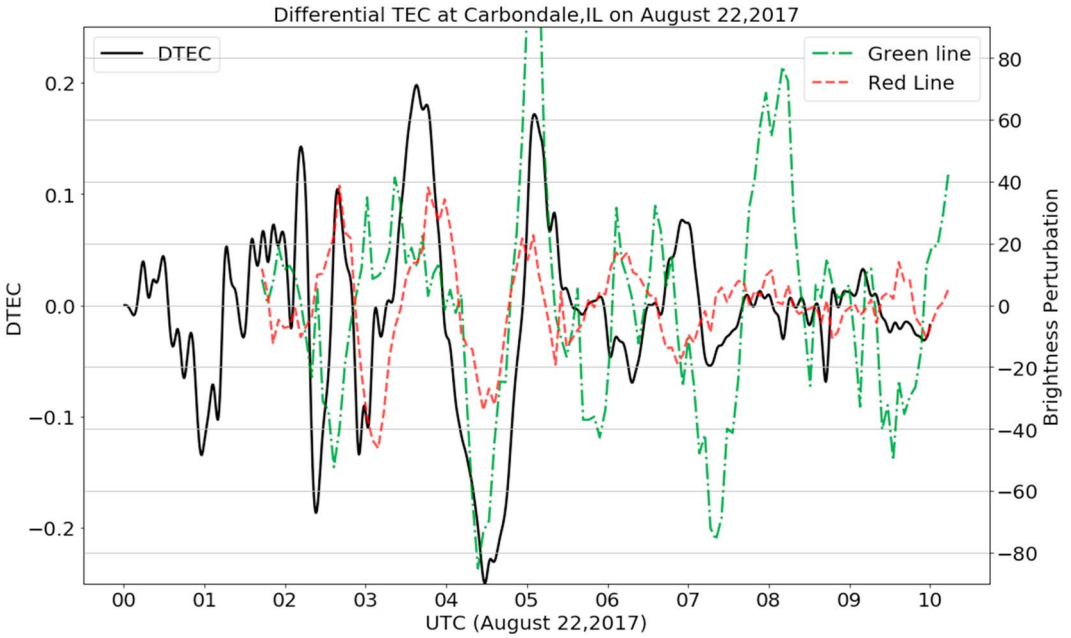

Figure 5. DTEC obtained for Carbondale, IL, on 22 August 2017 from Global Positioning System-derived TEC measurements (solid black lines). Notice stronger perturbations and better coincidence from 3–6 UTC (compared to the whole profile) with red and green line profiles shown in dash-dotted and dashed lines, respectively. This time frame also coincides with the stronger large-scale DTEC perturbation (Figure 4) and peak enhancement and recovery of the AE index (Figure 7). TEC = total electron content; DTEC = differential total electron content; UTC = universal time coordinated.

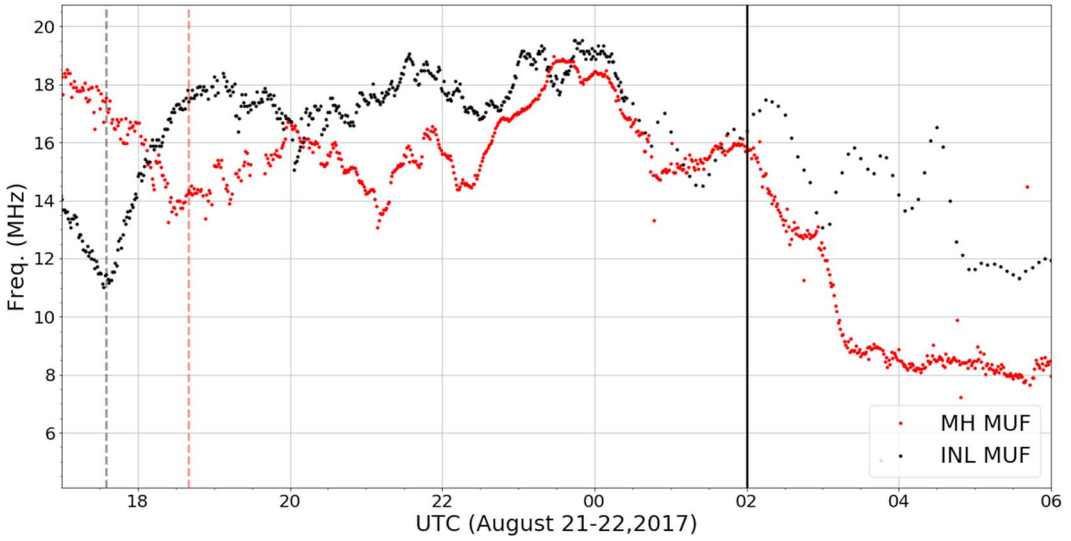

Figure 6. Digisonde-derived MUF series at Idaho National Lab (INL) and Millstone Hill (MH) from 17 UTC 21 August to 6 UTC 22 August 2017. INL was close to the path of the totality, and the 99% peak obscuration time is shown by the dashed vertical black line. MH was on the path of partial eclipse, and the 60% peak obscuration time is shown by the dashed vertical red line. High Throughput and Multi-slit Imaging Spectrograph observation starts around 2 UTC on 22 August, indicated by the vertical solid black line. UTC = universal time coordinated. UTC = universal time coordinated.

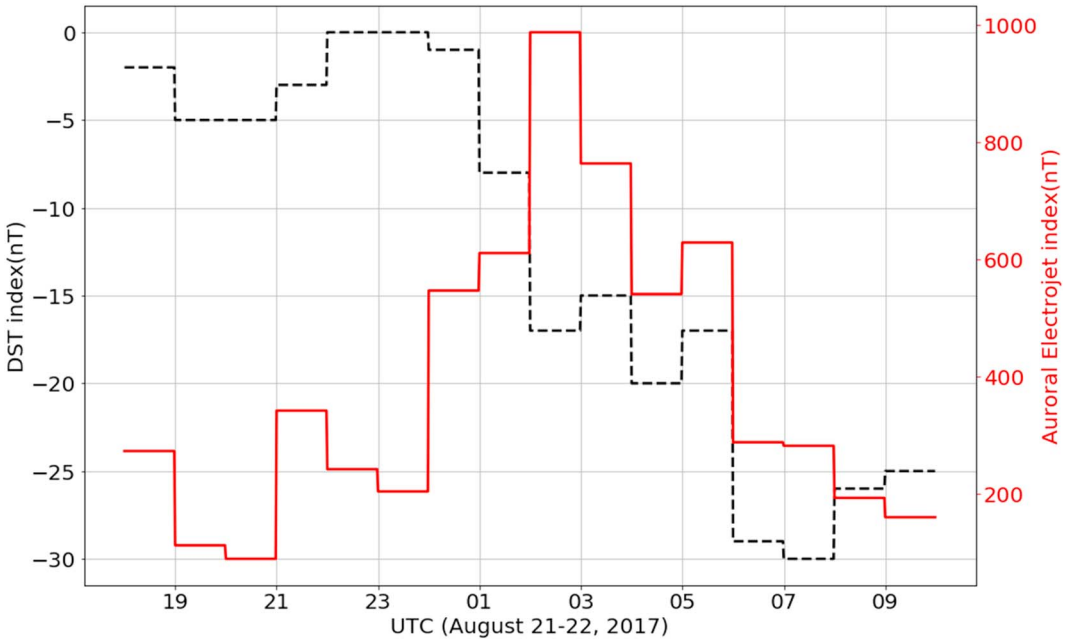

Figure 7. Dst and AE indices before and during High Throughput and Multi-slit Imaging Spectrograph observation times. Note the increase in AE starting at midnight UTC on 22 August 2017. UTC = universal time coordinated.

4. What Caused the Observed TIDs?

To understand the cause of the observed AGWs and TIDs, we analyzed the geomagnetic conditions. Figure 7 shows the Dst and the Auroral Electrojet (AE) indices from 18 UTC on 21 August to 10 UTC on 22 August 2017. The Dst index is a measure of the equatorial ring current strength and is obtained by averaging ground-based measurements of magnetic fields near the equator. The AE index is a measure of the strength of auroral currents and is obtained from magnetic field measurements near the polar cap. The AE strength is directly related to Joule heating of the IT system (Eyiguler et al., 2018) which, in turn, could potentially lead to equatorward propagating TIDs (see Kauristie et al., 2017, and references therein).

LSTIDs arrived over the FOV at about 1 UTC and lasted until around 6 UTC (Figure 5). Likewise, the AE index began to intensify at approximately the same time and relaxed back to prior values after 6 UTC (Figure 7). In addition, the keograms showed a complex structuring of the LSTIDs. The leading fronts initially arrived from the northeast and moved toward the southwest (1–4 UTC) but were almost perfectly elongated in the zonal direction later (4–6 UTC). TIDs in smaller scales within the LSTIDs can also be observed; these are most likely caused by wave breaking of the LSTIDs. We thus conclude that the observed LSTIDs (and AGWs) were most likely generated by geomagnetic effects that induced changes in the auroral current leading to rapid heating and expansion of the thermosphere.

5. Wave Characteristics

We performed wavelet analyses on the red and green line brightness profiles obtained at Carbondale, IL, digisonde MUF series obtained at INL and MH, and the DTEC measurements for Carbondale, IL. Wavelet analysis has been used by previous studies to identify wave characteristics of AGWs and TIDs (e.g., Kim & Chang, 2018; Singh & Pallamraju, 2016). Singh and Pallamraju (2016) studied the vertical propagation of AGWs due to a cyclone by performing wavelet analysis on optical emission brightnesses originating at different altitudes. Kim and Chang (2018) used wavelet analysis to study the variation in the geomagnetic field induced by eclipses.

The wavelet analysis is based on the guide presented in Torrence and Compo (1998) and implemented using the Waipy package on Python (https://github.com/mabelcalim/waipy). Red and green line brightness profiles averaged over the whole FOV were used as there was no significant change in dynamic behavior as a function of elevation angle (or latitude; see Figure 3). The average brightnesses and MUF series were sub-

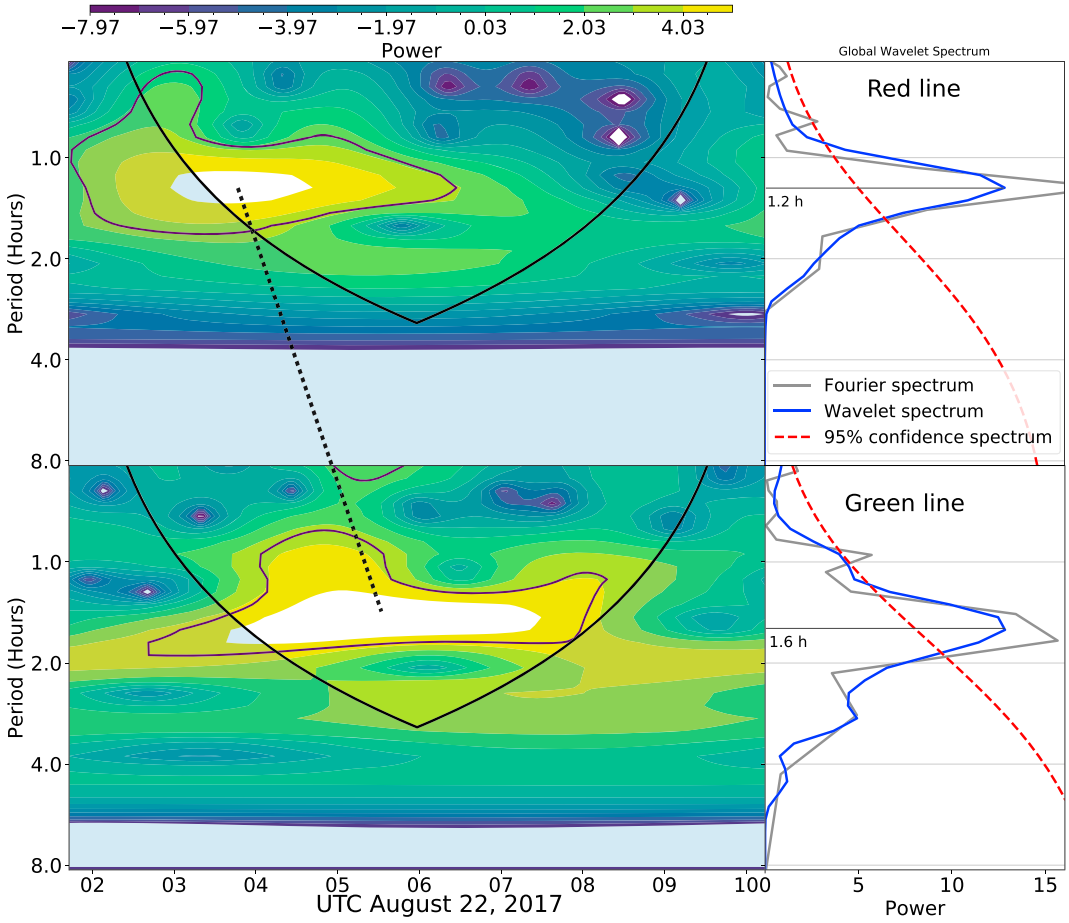

Figure 8. (left column) Wavelet analyses performed on the detrended red and green line brightnesses. A dominant wave period of 1.2 and 1.6 hr was found for the red and green lines, respectively. A black dashed line is shown to highlight the shift in peak time periods from the red to green line. The parabolic black line represents the cone of influence, below which the results are unreliable. The 95% confidence level powers on the wavelet spectra are represented by the dark purple contour. (right) The wavelet power spectrum averaged along all observation times and the corresponding fast Fourier transform power spectrum and wavelet spectrum are shown in gray and black, respectively. The 95% confidence interval for the global spectra are shown in red. UTC = universal time coordinated.

tracted with a polynomial fit in order to remove the long-term climatological trends. The extraction of the dynamic part of the TEC measurement, DTEC, has been described in section 2.2. These dynamic profiles were then zero mean, unit variance normalized, and the wavelet analysis was performed on these normalized values. Finally, the dominant time periods were obtained from the global wavelet spectra whose Full Width at Half Max was used to estimate the uncertainty.

The wavelet spectra for the red and green lines, shown in Figure 8, reveal a dominant wave period of 1.2 ± 0.5 hr for the red line and 1.6 ± 0.8 hr for the green line. However, the wavelet power for the red line peaked around 2–5 UTC and the green line wavelet power peaked around 3–6 UTC. The DTEC wavelet spectra show a dominant time period of 1.7 ± 0.7 hr and also has a peak around 3–6 UTC (Figure 9). The MUF wavelet spectra for both locations show similar dominant wave periods of around 1 hr (and other modes) with peaks at two different times (within 2–6 UTC, Figure 10). The wave period of 1 hr prior to midnight UTC (at MH) could be the aftereffect of the eclipse (as discussed earlier) since the perturbations precede geomagnetic disturbances.

The vertical phase speed (c_z) above the spectrograph was found to be 7 m/s estimated using the time delay obtained by performing cross-correlation analysis on the dynamic part of the red and green line profiles and the difference in their peak altitudes (250 and 220 km, respectively). The vertical wavelength, λ_z =

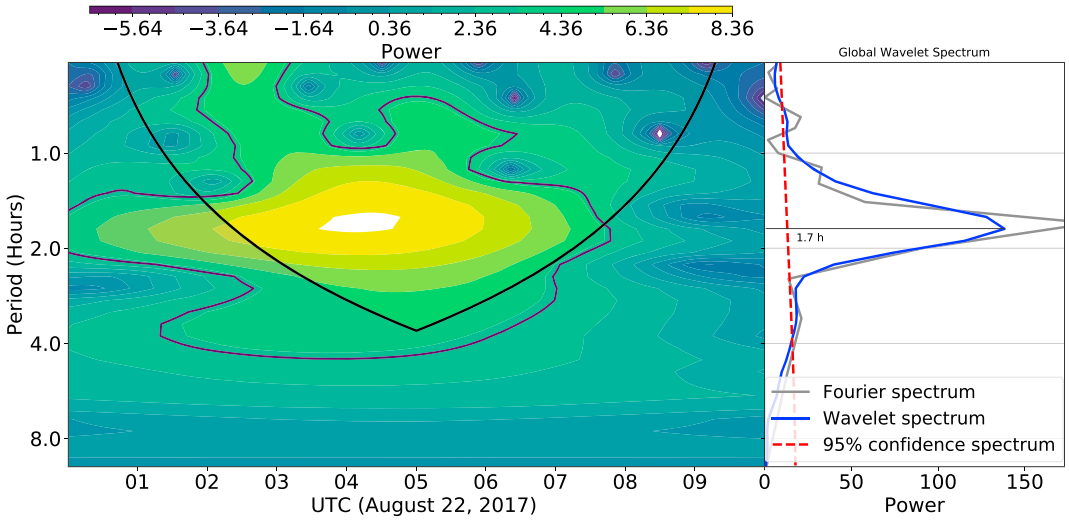

Figure 9. Wavelet analysis performed on the differential total electron content profile at Carbondale, IL, from Global Positioning System total electron content measurements. The dominant time period of 1.7 hr is seen starting around 4 UTC. UTC = universal time coordinated.

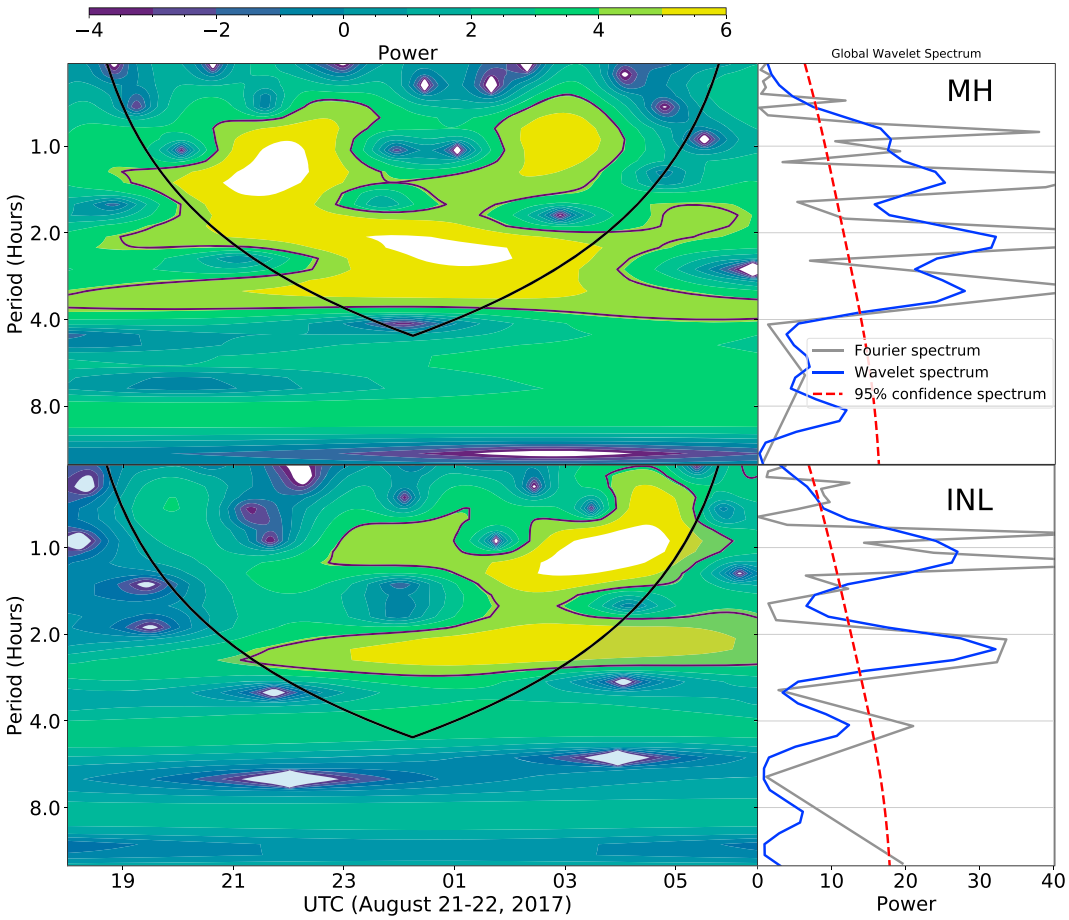

Figure 10. (left) Wavelet analysis performed on the dynamic part of the maximum usable frequency profiles from the MH (top) and INL (bottom). A dominant time period of 1 hr is seen at both locations at different times after midnight UTC is most likely associated with the enhancement in AE. Notice wavelet power spectrum with a dominant time period of 1 hr starting around 21 UTC at Millstone Hill which is before the commencement of the minor geomagnetic storm and could be associated with the aftereffect of the eclipse. MH = Millstone Hill; INL = Idaho National Laboratory; UTC = universal time coordinated.

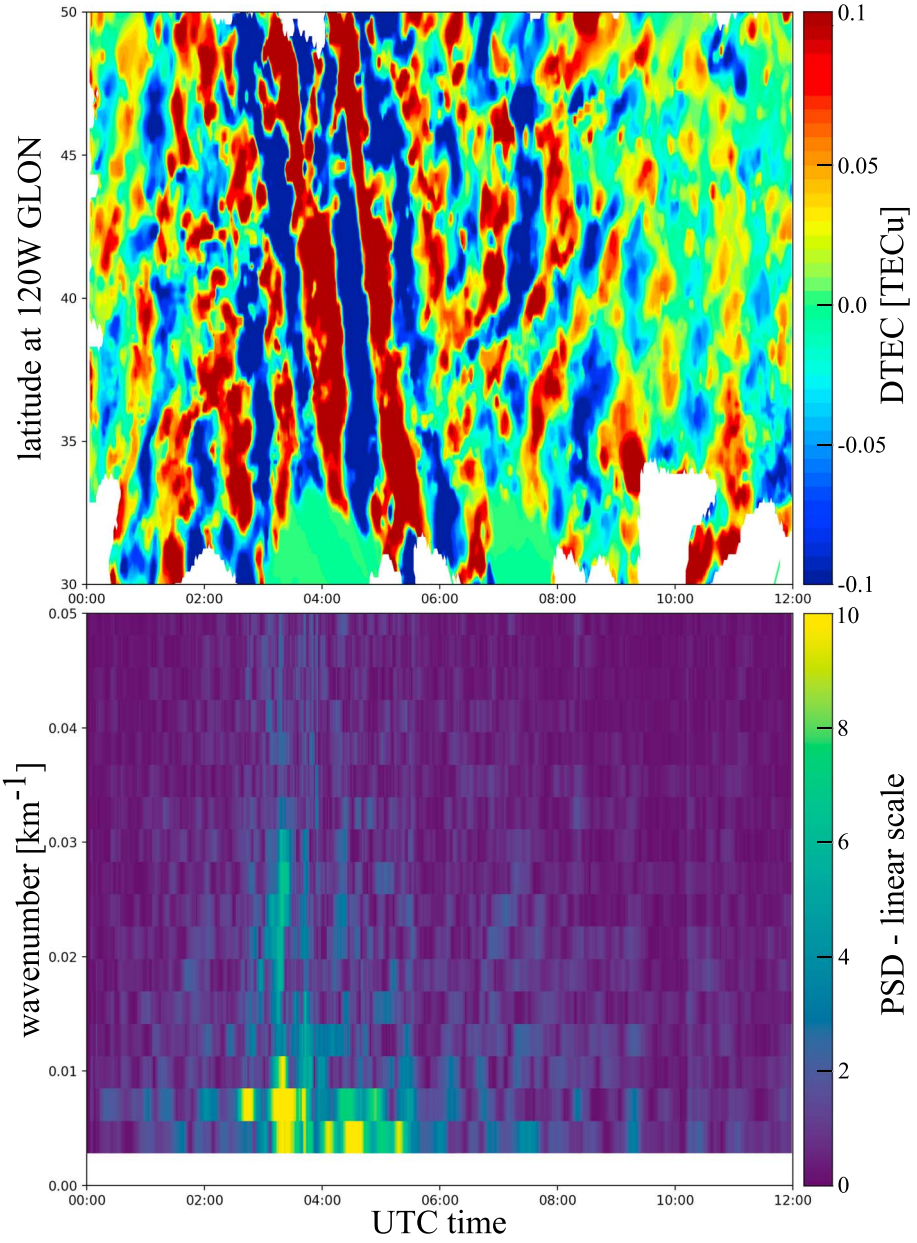

Figure 11. Large-scale traveling ionospheric disturbance analysis of meridional propagation velocity at 120°W (a) and meridional wavelength utilizing 2-D fast Fourier transform analysis (b). TEC = total electron content; DTEC = differential total electron content; UTC = universal time coordinated, GLON = Geographic Longitude, PSD = Power Spectral Density.

$c_z\tau_z$ = 36 km, was calculated using the average of the red and green line dominant wave time periods (τ_z = 1.4 hr) and the vertical phase speed (c_z = 7 m/s).

We used maps of DTEC to estimate horizontal wave parameters. Due to a longitudinal structuring of the LSTIDs, we used a latitudinal keogram elongated along 120°W, shown in Figure 11a. The slope of propagation was found to be 10° per 30 min, which translates to a meridional speed of 616 m/s, equatorward. A similar estimate was also made at Carbondale, IL, using the keogram in Figure 4. Spectral analysis (Mrak et al., 2018) was applied to the keogram in Figure 11a to obtain the dominant meridional wavenumber. The dominant meridional wavenumber is ~0.005 km^{-1} which translates to meridional wavelength λ_m = 1,256 km.

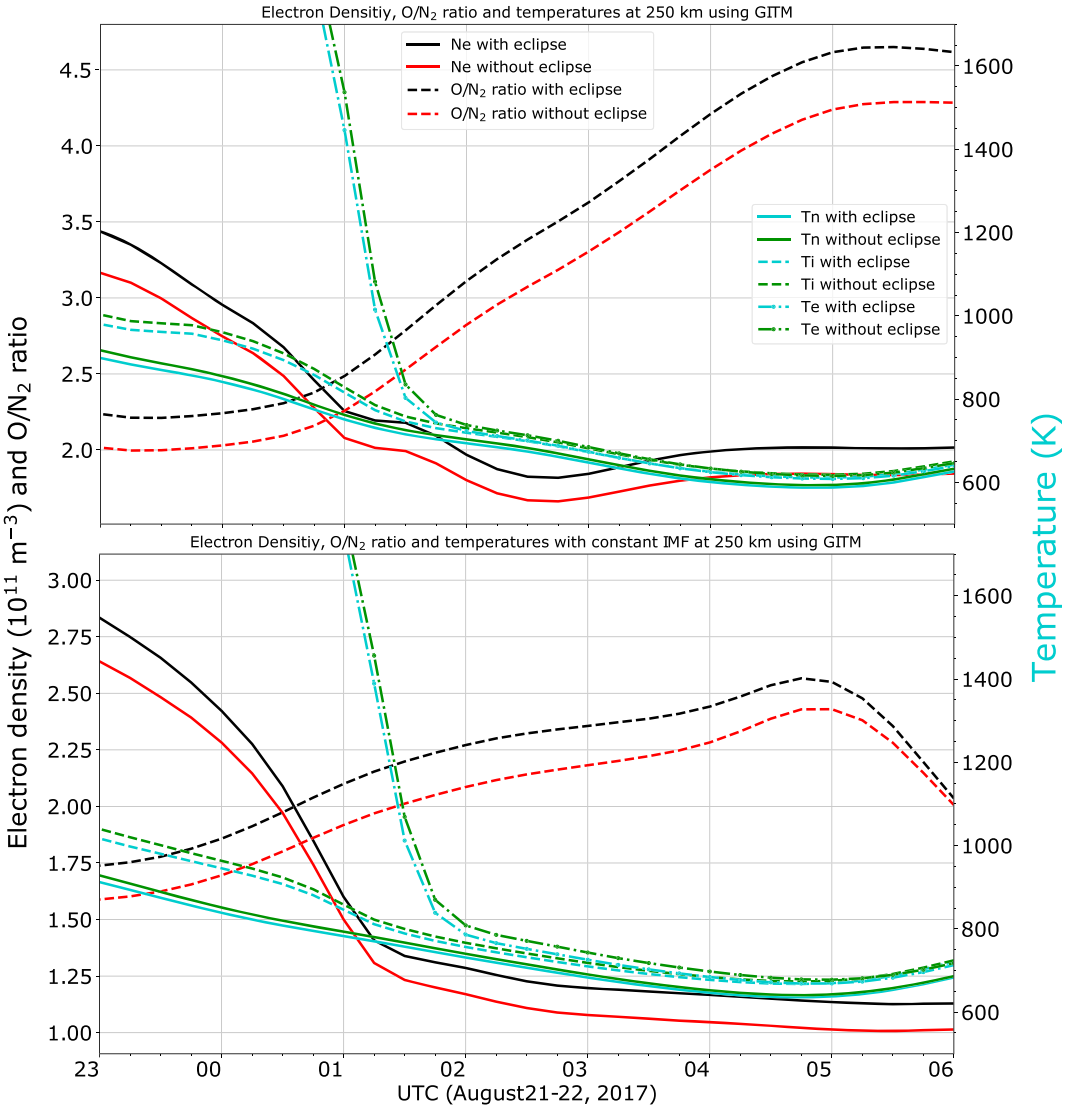

Figure 12. Electron densities (Ne), thermospheric O/N_2 ratio, and plasma and neutral temperatures at 250 km (peak of red line emission) as modeled by GITM for the eclipse and noneclipse (control) conditions with actual geomagnetic conditions (top) and constant geomagnetic conditions (bottom) at Carbondale, IL. While the profiles are very similar, electron density and the O/N_2 ratios are ~10% higher when the effects due the eclipse were included (for both actual and constant geomagnetic activity). All the temperatures (Tn: neutral temperature, Ti: ion temperature, Te: electron temperature) are slightly lower when the eclipse's effect is included. GITM = Global Ionosphere-Thermosphere Model; IMF = interplanetary magnetic field; UTC = universal time coordinated.

6. Effects of the Total Solar Eclipse on the Observed LSTIDs

A total solar eclipse had occurred 8 hr before the observed LSTIDs (at Carbondale, IL). While the LSTIDs were most likely generated by geomagnetic effects, the effect of a total solar eclipse on the IT system has also been well documented by recent and prior studies (e.g., Coster et al., 2017; Liu et al., 1998; Mrak et al., 2018). Furthermore, the MUF series at MH showed perturbations even prior to the start of the geomagnetically active time (Figure 6). This could potentially be due to the lingering effect of the eclipse.

To test the eclipse's effect for our observations, the GITM (Ridley et al., 2006) was used to simulate the effects of the 21 August 2017 eclipse on the IT system. The Flare Irradiance Spectral Model (Chamberlin et al., 2007) was used to specify the solar EUV (extreme ultraviolet) spectrum, but this was modified to reduce the EUV heating and ionization in the region of the lunar occultation of the Earth to simulate the eclipse effect. This was done as described by Wu et al. (2018), although they used a different EUV model. The path of the

eclipse was defined in geocentric solar ecliptic (GSE) coordinates as a straight line in the (Y_{GSE}, Z_{GSE}) plane, assuming X_{GSE} constant. The reduction in EUV irradiance was based on the distance between each GITM grid point and the center of totality; at the center of totality, the EUV irradiance was reduced to 10% of the normal value, which linearly increased until the edge of the occultation region was approached, after which the EUV increased exponentially back to 100% at 3,800-km distance from the center of totality.

Four simulations were performed. First, a set of two simulations were run with observed IMF and solar wind data to drive the high-latitude electric potential and auroral precipitation patterns. One of these simulations included the effects of the eclipse, while the other (the control run) did not. To test the influence of variable geomagnetic activity on the results, an additional set of simulations (eclipse and control) were run with actual solar wind conditions and constant IMF, that is, fixed geomagnetic activity. For these two simulations with constant IMF, the following solar wind and IMF parameters were used: solar wind speed = −534 km/s, solar wind density = 4.0 cm^{-3}, B_x = −3.1 nT, B_y = −2.3 nT, and B_z = −3.0 nT. All the simulations were otherwise set up identically. The model was run with a resolution of 2.0° in latitude, 4.0° in longitude, and ~0.3 times the scale height in altitude, spanning from 100 km to approximately 600-km altitude. The simulations with observed solar wind and IMF parameters used here are the same as those analyzed by Cnossen et al. (in review), who describe the simulation setup in further detail.

Figure 12 shows the electron density, the thermospheric O/N_2 ratios, and plasma and neutral temperatures estimated using GITM at 250 km, which is where the red line emission peaks, for the four cases: with and without the effect of the eclipse for actual and constant geomagnetic activity. The electron density and the O/N_2 ratio were around 10% higher when the eclipse's effects were included, but the time profile was very similar to the noneclipse case for both geomagnetic activity conditions. All the temperatures are slightly lower (compared to density changes) when the eclipse's effect is considered. For actual geomagnetic activity conditions, there is a slight enhancement in the electron density between 1 and 2 UT, but no wave-like perturbation is seen. While the results imply that the IT system is preconditioned even hours after the eclipse event, no LSTIDs are observed with the simulations for any of the selected conditions. We thus conclude that there is no evidence that the eclipse had any effect on the observed LSTIDs, although we cannot completely rule out such effects, since the model did not reproduce the observed LSTIDs for any of the simulated cases.

7. Discussion

Wave-like structures were observed in red and green line emissions and GPS TEC measurements at Carbondale, IL, as well as in digisonde measurements at INL and MH. These observations showed that the dynamic part of the red and green lines and the DTEC profiles at Carbondale, IL, coincided best around 3–6 UTC (22 August 2017; Figure 5), which is also when the DTEC keogram shows prominent LSTIDs (Figure 4c). All of the wavelet spectra also have a similar dominant wave power around the same time frame (3–6 UTC). In addition, the AE index peaks and recovers during the same time period too (Figure 7). This indicates that the increase in auroral currents and associated Joule heating near the poles were responsible for the observed LSTIDs. There are TIDs prior to and after 3–6 UTC in the DTEC map (Figure 4c); however, their scale sizes are smaller and they are weaker.

Multispectral observation from HiT&MIS would have been sufficient to infer the vertical wave characteristics of the TID. However, the brightness perturbation spanned its FOV, so the meridional scale size of the TID could not have been estimated. Similarly, using the DTEC measurements, meridional wave characteristics could have been estimated but not the vertical wave characteristics. Thus, by using multiple measurements in combination, we were able to do a more comprehensive analysis of the wave properties than would have been possible with individual measurements in isolation.

The estimated dominant wave time periods are slightly different for different observations, that is, 1.2 ± 0.5, 1.6 ± 0.8, and 1.7 ± 0.7 hr for the red line, green line, and DTEC, respectively at Carbondale, IL. The dominant wave period of around 1 hr was also found for MUF series at both INL and MH. MUF is sensitive to the bottomside ionospheric plasma densities; the red and green line brightnesses are sensitive to both the plasma and the neutral densities at the altitude they peak at, and the TEC measurements are sensitive to the line-of-sight ionospheric plasma density. These differences could explain the minor discrepancy in dominant time periods.

Previous studies have observed disturbances in the IT system well after the eclipse and far away from its path (e.g., Harding et al., 2018; Verhulst & Stankov, 2018). Goncharenko et al. (2018) reported enhanced electron density (>50–150%) starting from 21 UTC, 21 August 2017 to at least midnight UTC (22 August) based on radar measurements at MH hours after the eclipse. The authors attributed this enhancement in electron density to the downward flux of plasma from the plasmasphere that was initially filled by upwelling of plasma immediately following the eclipse. This electron density enhancement was not predicted by GITM, as it does not include contributions from the plasmasphere. The 21–22 UTC is also when one of the peaks in the MUF wavelet spectrum with a dominant wave time period of around 1 hr at MH is observed (Figure 10). This indicates that the observed perturbation in MUF was caused by an eclipse-related effect with a similar time period of around 1 hr as was observed later, probably in relation to geomagnetic disturbance effects. Wu et al. (2018) reported that the IT system's response to the eclipse in GITM decays much quicker than is seen in TEC and *NmF*2 observations. On the other hand, a 10% increase in both O/N_2 ratio and N_e at Carbondale, IL, predicted by GITM is consistent with the quantitative enhancement in red line brightness we observed when compared to the night before (see supporting information Figure S2). However, GITM failed to produce the wave-like perturbations seen in red and green line airglow brightnesses, possibly due to coarser resolution in latitude and longitude. Thus, it is possible that the eclipse's long-term effect not only influenced the TID strength but also could have interacted with the geomagnetic effects in the formation of the observed LSTIDs. However, based on this study, we could only conclude that while the eclipse effects were still present during the LSTID events, they had no detectable impact on the observed LSTIDs.

8. Summary

We have presented an analysis of wave-like perturbations observed in red and green line brightnesses from ground-based optical measurements. Additional insight was provided by MUF series based on digisonde measurements and GPS-based TEC measurements. We conclude that a geomagnetic disturbance starting at midnight UTC on 22 August 2017 enhanced the auroral currents that lead to Joule heating which triggered AGWs and associated LSTIDs propagating toward the equator. Furthermore, a total solar eclipse had occurred hours earlier over the continental United States (8 hr earlier in Carbondale, IL). By using the GITM simulations, we found that preconditioning of the IT system due to eclipse increased N_e and the O/N_2 ratio at 250 km around 10% during the observed TID event but does not seem to effect the LSTIDs. Wavelet analysis performed on all the measurements shows a similar dominant time period of about 1.5 hr. Using cross-correlation analysis on the red and green line brightness profiles, the vertical phase speed was found to be 7 m/s, corresponding to a vertical wavelength of 36 km. Similarly, spectral analysis of DTEC keogram was used to estimate the meridional phase speed of 616 m/s, corresponding to a meridional wavelength of 1,256 km.

Acknowledgments
This work was partially supported by the NSF grant AGS1145166 and UMass Lowell internal funds. Sebastijan Mrak was supported by NSF grant AGS-1743832 to Boston University. Dr. Ingrid Cnossen was supported by NSF grant ATM1452097. She can be contacted for any GITM runs. GITM simulations were performed on the NASA Pleiades high-performance computing facilities. The brightness data from HiT&MIS used for this work are available online (10.5281/zenodo.1494258). Digisonde data were retrieved from online DIDBase repository of the Global Ionosphere Radio Observatory (GIRO) via its SAO Explorer workstations and at http://giro.uml.edu portal. Digisonde data from Idaho National Laboratory are courtesy of Dr. James R. Hanneman. We thank Dr. Stan Solomon at UCAR/NCAR for constructive discussions on the GLOW model whose Python wrapped version can be found online (github.com/scivision/glowaurora).

References

Altadill, D., Belehaki, A., Blanch, E., Borries, C., Buresova, D., Galkin, I., et al. (2018). Report on TID algorithms.

Aryal, S., Finn, S. C., Hewawasam, K., Maguire, R., Geddes, G., Cook, T., et al. (2018). Derivation of the energy and flux morphology in an aurora observed at midlatitude using multispectral imaging. *Journal of Geophysical Research: Space Physics*, *123*, 4257–4271. https://doi.org/10.1029/2018JA025229

Azeem, I., Yue, J., Hoffmann, L., Miller, S. D., Straka, W. C., & Crowley, G. (2015). Multisensor profiling of a concentric gravity wave event propagating from the troposphere to the ionosphere. *Geophysical Research Letters*, *42*, 7874–7880. https://doi.org/10.1002/2015GL065903

Bailey, S. M., Barth, C. A., & Solomon, S. C. (2002). A model of nitric oxide in the lower thermosphere. *Journal of Geophysical Research*, *107*(A8), 1205. https://doi.org/10.1029/2001JA000258

Chakrabarti, S., Jokiaho, O.-P., Baumgardner, J., Cook, T., Martel, J., & Galand, M. (2012). High-throughput and multislit imaging spectrograph for extended sources. *Optical Engineering*, *51*(1), 013003–1. https://doi.org/10.1117/1.OE.51.1.013003

Chamberlin, P. C., Woods, T. N., & Eparvier, F. G. (2007). Flare irradiance spectral model (FISM): Daily component algorithms and results. *Space Weather*, *5*, S07005. https://doi.org/10.1029/2007sw000316

Chimonas, G., & Hines, C. (1970a). Atmospheric gravity waves induced by a solar eclipse. *Journal of Geophysical Research*, *75*(4), 875–875.

Chimonas, G., & Hines, C. O. (1970b). Atmospheric gravity waves launched by auroral currents. *Planetary and Space Science*, *18*(4), 565–582. https://doi.org/10.1016/0032-0633(70)90132-7

Coster, A. J., Gaposchkin, E. M., & Thornton, L. E. (1992). Real-time ionospheric monitoring system using GPS. *Navigation*, *39*(2), 191–204.

Coster, A. J., Goncharenko, L., Zhang, S.-R., Erickson, P. J., Rideout, W., & Vierinen, J. (2017). GNSS observations of ionospheric variations during the 21 August 2017 solar eclipse. *Geophysical Research Letters*, *44*, 12,041–12,048. https://doi.org/10.1002/2017GL075774

Coster, A., Herne, D., Erickson, P., & Oberoi, D. (2012). Using the Murchison Widefield array to observe midlatitude space weather. *Radio Science*, *47*, RS0K07. https://doi.org/10.1029/2012RS004993

Davies, K. (1989). *Ionospheric radio (ionospheric radio wave propagation)*. Boulder, CO: Peter Peregrinus.

Davis, M. J. (1971). On polar substorms as the source of large-scale traveling ionospheric disturbances. *Journal of Geophysical Research*, *76*(19), 4525–4533. https://doi.org/10.1029/JA076i019p04525

Eyiguler, E. C. Kalafatoglu, Kaymaz, Z., Frissell, N. A., Ruohoniemi, J. M., & Rastätter, L. (2018). Investigating upper atmospheric Joule heating using cross-combination of data for two moderate substorm cases. *Space Weather*, *16*, 987–1012. https://doi.org/10.1029/2018SW001956

Goncharenko, L. P., Erickson, P. J., Zhang, S.-R., Galkin, I., Coster, A. J., & Jonah, O. F. (2018). Ionospheric response to the solar eclipse of 21 August 2017 in Millstone Hill (42N) observations. *Geophysical Research Letters*, *45*, 4601–4609. https://doi.org/10.1029/2018GL077334

Habarulema, J. B., Yizengaw, E., Katamzi-Joseph, Z. T., Moldwin, M. B., & Buchert, S. (2018). Storm time global observations of large-scale TIDs from ground-based and in situ satellite measurements. *Journal of Geophysical Research: Space Physics*, *123*, 711–724. https://doi.org/10.1002/2017JA024510

Harding, B. J., Drob, D. P., Buriti, R. A., & Makela, J. J. (2018). Nightside detection of a large-scale thermospheric wave generated by a solar eclipse. *Geophysical Research Letters*, *45*, 3366–3373. https://doi.org/10.1002/2018GL077015

Hines, C. O. (1960). Internal atmospheric gravity waves at ionospheric heights. *Canadian Journal of Physics*, *38*(11), 1441–1481. https://doi.org/10.1139/p60-150

Hocke, K., & Schlegel, K. (1996). A review of atmospheric gravity waves and travelling ionospheric disturbances: 1982–1995. *Annales Geophysicae*, *14*(9), 917.

Kauristie, K., Morschhauser, A., Olsen, N., Finlay, C. C., McPherron, R. L., Gjerloev, J. W., & Opgenoorth, H. J. (2017). On the usage of geomagnetic indices for data selection in internal field modelling. *Space Science Reviews*, *206*(1), 61–90. https://doi.org/10.1007/s11214-016-0301-0

Kelley, M. C. (2011). On the origin of mesoscale TIDs at midlatitudes. *Annales Geophysicae*, *29*(2), 361–366.

Kim, J.-H., & Chang, H.-Y. (2018). Geomagnetic field variations observed by INTERMAGNET during 4 total solar eclipses. *Journal of Atmospheric and Solar-Terrestrial Physics*, *172*, 107–116. https://doi.org/10.1016/j.jastp.2018.03.023

Klobuchar, J. A. (1987). Ionospheric time-delay algorithm for single-frequency GPS users: AIR FORCE SYSTEMS COMMAND HANSCOM AFB MA GEOPHYSICS LAB.

Lin, C. Y., Deng, Y., & Ridley, A. (2018). Atmospheric gravity waves in the ionosphere and thermosphere during the 2017 solar eclipse. *Geophysical Research Letters*, *45*, 5246–5252. https://doi.org/10.1029/2018GL077388

Liu, J. Y., Hsiao, C. C., Tsai, L. C., Liu, C. H., Kuo, F. S., Lue, H. Y., & Huang, C. M. (1998). Vertical phase and group velocities of internal gravity waves derived from ionograms during the solar eclipse of 24 October 1995. *Journal of Atmospheric and Solar-Terrestrial Physics*, *60*(17), 1679–1686. https://doi.org/10.1016/S1364-6826(98)00103-5

Lowell Digisonde International (LDI) (2018). Digisonde DPS4D Manual.

Mrak, S., Semeter, J., Drob, D., & Huba, J. D. (2018). Direct EUV/X-ray modulation of the ionosphere during the August 2017 total solar eclipse. *Geophysical Research Letters*, *45*, 3820–3828. https://doi.org/10.1029/2017GL076771

Mrak, S., Semeter, J., Nishimura, Y., Hirsch, M., & Sivadas, N. (2018). Coincidental TID production by tropospheric weather during the August 2017 total solar eclipse. *Geophysical Research Letters*, *45*, 10,903–10,911. https://doi.org/10.1029/2018GL080239

Munro, G. (1950). Travelling disturbances in the ionosphere. *Proceedings of the Royal Society A*, *202*(1069), 208–223.

Prölss, G. W., & Ocko, M. (2000). Propagation of upper atmospheric storm effects towards lower latitudes. *Advances in Space Research*, *26*(1), 131–135. https://doi.org/10.1016/S0273-1177(99)01039-X

Reinisch, B. W., & Galkin, I. A. (2011). Global ionospheric radio observatory (GIRO). *Earth, Planets and Space*, *63*(4), 377–381.

Reinisch, B. W., Galkin, I. A., Khmyrov, G., Kozlov, A., Bibl, K., Lisysyan, I., et al. (2009). New digisonde for research and monitoring applications. *Radio Science*, *44*, RS0A24. https://doi.org/10.1029/2008RS004115

Ridley, A. J., Deng, Y., & Toth, G. (2006). The global ionosphere thermosphere model. *Journal of Atmospheric and Solar-Terrestrial Physics*, *68*(8), 839–864.

Singh, R. P., & Pallamraju, D. (2016). Effect of cyclone Nilofar on mesospheric wave dynamics as inferred from optical nightglow observations from Mount Abu, India. *Journal of Geophysical Research: Space Physics*, *121*, 5856–5867. https://doi.org/10.1002/2016JA022412

Solomon, S. C., & Abreu, V. J. (1989). The 630 nm dayglow. *Journal of Geophysical Research*, *94*(A6), 6817–6824.

Solomon, S. C., Hays, P. B., & Abreu, V. J. (1988). The auroral 6300 emission: Observations and modeling. *Journal of Geophysical Research*, *93*, 9867–9882. https://doi.org/10.1029/JA093iA09p09867

Torrence, C., & Compo, G. P. (1998). A practical guide to wavelet analysis. *Bulletin of the American Meteorological society*, *79*(1), 61–78.

Verhulst, T. G., & Stankov, S. M. (2018). Ionospheric wave signature of the American solar eclipse on 21 August 2017 in Europe. *Advances in Space Research*, *61*(9), 2245–2251.

Wu, C., Ridley, A. J., Goncharenko, L., & Chen, G. (2018). GITM-data comparisons of the depletion and enhancement during the 2017 solar eclipse. *Geophysical Research Letters*, *45*, 3319–3327. https://doi.org/10.1002/2018GL077409